Chalcogenide Letters

Tech Science Press

http://doi.org/10.32604/cl.2026.082986

ARTICLE

Zn Vacancy-Regulated $Zn_{0.4}Cd_{0.6}S$ for Enhanced Charge Separation and Boosted Photocatalytic H_2O_2 Generation

Yuanyi Zhang, Yang Gu, Yuxin Lan, Zhenyu Wang, Wei Yan, Yingcong Wei and Jing Xu*

School of Physics and Electronic Engineering, Jiangsu University, Zhenjiang, 212013, China
*Corresponding Author: Jing Xu. Email: xjing@ujs.edu.cn

Received: 26 March 2026; Accepted: 20 May 2026; Published: 02 June 2026

ABSTRACT: Photocatalytic H_2O_2 synthesis from O_2 is a green and environmentally friendly route. However, due to the limitations of quick recombination of photogenerated electrons and limited O_2 activation ability, photocatalytic reactions often exhibit low efficiency. In this study, Zn vacancy-engineered $Zn_{0.4}Cd_{0.6}S$ (Zn_V-ZCS) photocatalysts were successfully constructed via a hydrothermal strategy using L-cysteine as a coordination agent. The optimized Zn_V-ZCS-10 catalyst achieves an impressive H_2O_2 production rate of 44.39 mmol/g within 1 h under 425 nm irradiation, approximately 2.3 times higher than that of pristine $Zn_{0.4}Cd_{0.6}S$ (ZCS). Structural characterization and cycling performance tests confirm that the introduction of Zn vacancies does not alter the pristine hexagonal crystal phase of the material, demonstrating good stability. Photoelectrochemical and spectroscopic analyses reveal that Zn vacancies effectively enhance charge carrier separation and reduce charge transfer resistance. Meanwhile, the presence of cation vacancies reconstructs the local electronic environment, promoting the activity of the $Zn_{0.4}Cd_{0.6}S$ catalyst for H_2O_2 production via the superoxide radical ($\cdot O_2^-$)-mediated pathway. This work highlights the crucial role of cation vacancies in modulating carrier dynamics in sulfide semiconductors for efficient photocatalytic H_2O_2 production.

KEYWORDS: $Zn_{0.4}Cd_{0.6}S$; cation vacancies; Zn vacancies; photocatalytic H_2O_2 production

1 Introduction

Hydrogen peroxide (H_2O_2) is a recognized environment-friendly selective oxidant, which has a large number of applications in the fields of environmental remediation and organic synthesis [1], and is also widely used in pollutant degradation and scenarios such as bacterial inactivation [2–6]. Under mild reaction conditions, the use of semiconductor materials for the photocatalytic H_2O_2 yield is always regarded as a green solution to replace the anthraquinone process [7–10], but under visible light illumination, the swift recombination of photoinduced charges and the insufficient O_2 activation capability and inefficient interfacial reduction kinetics limit the rate of photocatalytic generation of H_2O_2. Therefore, it is difficult to improve selectivity [11–15].

Benefiting from an adjustable electronic energy band configuration and excellent visible-light responsiveness, $Zn_xCd_{1-x}S$ solid solution has received extensive attention in the study of photocatalytic production of H_2O_2 [16–20]. However, due to the limitations in O_2 adsorption/activation, $Zn_xCd_{1-x}S$ photocatalysts still face challenges in achieving higher H_2O_2 yield and selectivity [21–24]. Introducing cation vacancies such as Zn vacancies into the lattice is an effective way to reshape the local electronic environment and optimize interfacial charge behavior [25–30], as it can reconstruct local electron density and alter adsorption/activation properties. Ding et al. systematically reviewed the regulatory mechanisms

of cation vacancies (e.g., Zn and In vacancies) in photocatalysis and electrocatalysis, highlighting that they can modulate reaction kinetics by reconstructing local electron density and optimizing adsorption configurations [31]. Yu et al. further summarized the roles of cation vacancies in regulating catalytic processes through electronic structure reconstruction and adsorption optimization [32]. Wang et al. comprehensively outlined the influence of defect engineering, ranging from atomic-scale vacancies to macroscopic structural regulation, on electronic band structure alignment and recombination kinetics of carriers [33]. Therefore, tailoring the carrier kinetics in ZCS and enhancing the selectivity towards the key intermediate $\cdot O_2^-$ by constructing cationic Zn vacancies is an effective approach to promote the two-step single-electron reduction pathway for H_2O_2 production.

In this work, Zn vacancies (Zn_V) are added into the $Zn_{0.4}Cd_{0.6}S$ (ZCS) lattice by a hydrothermal method. This process is based on the strong coordination interaction between Zn^{2+} and the thiol (-SH) group of L-cysteine. The optimized Zn_V-ZCS-10 sample exhibits significantly enhanced photocatalytic performance for H_2O_2 production. Its activity is markedly higher than that of the pristine sample, showing over 2.3-fold improvement. In addition, the catalyst demonstrates good stability, retaining most of its initial activity after repeated cycling tests. Adding Zn vacancies still keeps the main crystal phase of the material. At the same time, it facilitates charge-carrier separation and changes the band structure. EPR results, radical trapping tests, and atmosphere tests demonstrate that Zn_V-$Zn_{0.4}Cd_{0.6}S$-10 undergoes the oxygen reduction reaction proceeding via a two-step single-electron reduction. The superoxide radical ($\cdot O_2^-$) serves as a key intermediate in this reaction. This work gives a simple way to design sulfide photocatalysts with cation vacancies for H_2O_2 synthesis.

2 Results and Discussion

2.1 Catalyst Structural Analysis

The synthesis process of Zn_V-ZCS is shown in Fig. 1a. We use zinc acetate dihydrate, cadmium acetate dihydrate and L-cysteine as raw materials, Zn_V-ZCS samples were synthesized in hydrothermal environment with the strong coordination of Zn and L-cysteine mercapto (-SH). Scanning electron microscope (SEM) images (Fig. S1) show that both pure ZCS and Zn_V-ZCS-10 are granular morphology; Transmission electron microscope (TEM) (Fig. 1b) further observed that, Zn_V-ZCS-10 consists of numerous nanoparticles exhibiting amorphous-shaped morphology and dimensions of several tens of nanometers. Compared with pure ZCS (Fig. S2), the overall morphology has no obvious change, this shows that the introduction of vacancy does not cause large-scale structural damage to particles. High-Resolution Transmission Electron Microscopy (HRTEM) (Fig. 1c) clearly exhibits well-resolved lattice fringes showing an interplanar distance of approximately 0.33 nm, this matches the (002) crystallographic plane of $Zn_{0.4}Cd_{0.6}S$, indicating that the overall crystallinity is largely preserved. High-Angle Annular Dark-Field Scanning Transmission Electron Microscopy (HAADF-STEM) was used to characterize the morphology, while elemental mapping was applied to reveal the spatial distribution of elements (Fig. 1d). They illustrate that S, Zn, and Cd are homogeneously distributed throughout the particles, implying that the detected defects are predominantly atomic-scale point defects. X-ray Diffraction (XRD) (Fig. 1e) demonstrates that ZCS and Zn_V-ZCS-10 possess the same hexagonal phase (PDF#40-0836). The diffraction peaks of Zn_V-ZCS-10 become slightly wider and weaker. This suggests a small decrease in crystallinity. This change is due to the presence of Zn vacancies in Zn_V-ZCS-10. In the EPR spectrum, Zn_V-ZCS-10 exhibits a distinct signal at g = 2.004, whereas pristine ZCS shows a negligible response at this position. This signal is reasonably attributed to unpaired electrons associated with defect centers related to Zn vacancies [34–36]. ICP analysis indicates that the concentration of Zn vacancies in Zn_V-ZCS-10 is approximately 4.1226 wt%.

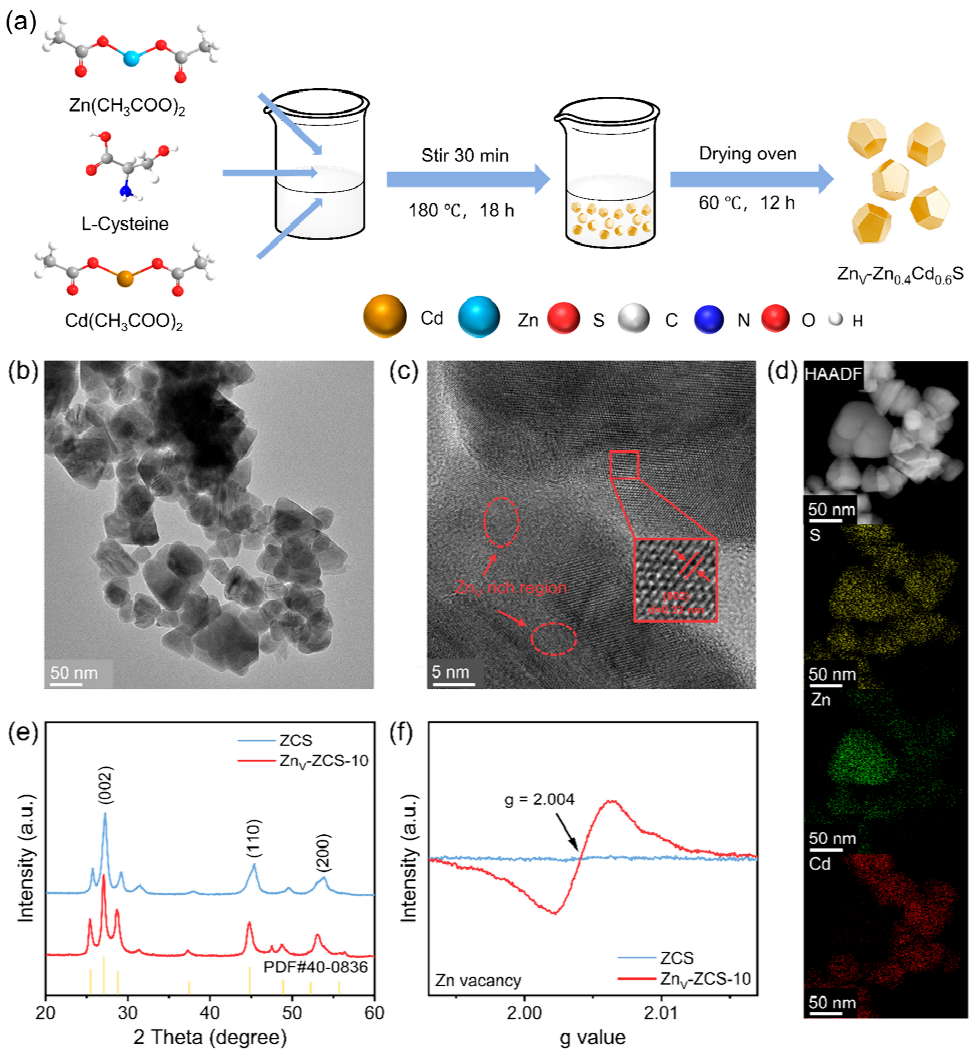

Figure 1: (**a**) Schematic diagram of the preparation of Zn_V-ZCS-10; (**b**) TEM image of Zn_V-ZCS-10; (**c**) HRTEM images of Zn_V-ZCS-10; (**d**) HAADF-STEM image and elemental mapping of Zn_V-ZCS-10; (**e**) XRD patterns of ZCS and Zn_V-ZCS-10; (**f**) EPR spectra of ZCS and Zn_V-ZCS-10.

XPS measurements were conducted to elucidate the surface chemical environments of the samples (Fig. 2a–d). As shown in Fig. 2a, the survey spectrum reveals the existence of S, Zn, Cd, C and O. For the high-resolution S 2p spectrum (Fig. 2b), the peaks at 161.27 eV and 162.50 eV can be assigned to S $2p_{3/2}$ and S $2p_{1/2}$, respectively, indicating the typical sulfide S^{2-} state. In Fig. 2c, the Zn 2p peaks centered at 1021.73 eV and 1044.71 eV are attributed to Zn $2p_{3/2}$ and Zn $2p_{1/2}$, confirming the Zn^{2+} state. Meanwhile, the Cd 3d spectrum in Fig. 2d shows two peaks at 404.83 eV and 411.58 eV, corresponding to Cd $3d_{5/2}$ and Cd $3d_{3/2}$, which suggests that Cd mainly exists as Cd^{2+}. Overall, the XPS results demonstrate that the chemical states of the elements in the sample remain essentially unchanged. The C 1s peak mainly arises from adventitious carbon and was used for binding-energy calibration, whereas the O 1s signal can be attributed to surface-adsorbed oxygen-containing species, such as hydroxyl groups or adsorbed water [37–39]. From the XPS results, it can be seen that the Zn 2p and Cd 3d peaks in Zn_V-ZCS-10 shift toward higher binding energy compared to those in ZCS, while the S 2p peak shifts toward lower binding energy. This indicates that Zn vacancies modulate the surface electronic structure of Zn_V-ZCS-10, leading

to electron enrichment on the S atoms. The surface element content table (Table S3) obtained from XPS analysis shows that the Zn content in Zn_V-ZCS-10 is lower than that in ZCS, confirming the introduction of Zn vacancies in Zn_V-ZCS-10.

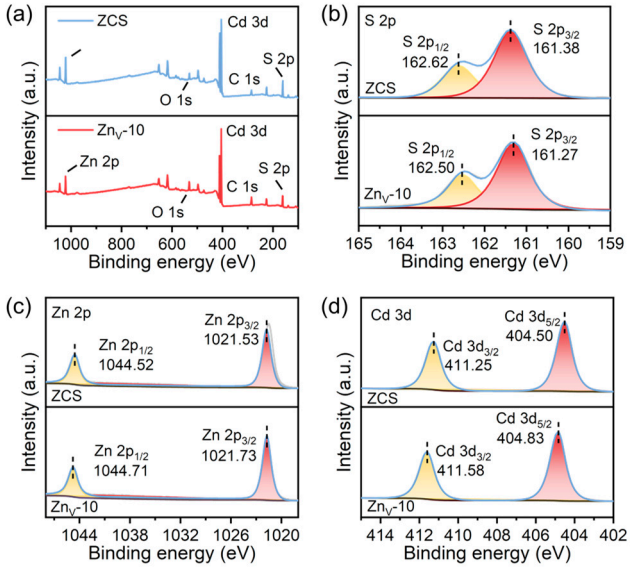

Figure 2: XPS characterization of ZCS and Zn_V-ZCS-10: (**a**) survey spectra; (**b**) high-resolution S 2p spectra; (**c**) high-resolution Zn 2p spectra; (**d**) high-resolution Cd 3d spectra.

2.2 Photocatalytic H_2O_2 Production Performance

Quantitative evaluation of photocatalytic H_2O_2 production was carried out according to the calibration curve provided in Fig. S5. Under the identical experimental conditions, in one hour, the production amount of H_2O_2 in pure ZCS sample was 19.25 mmol/g, while the production amount of Zn_V-ZCS-10 reached 44.39 mmol/g, which is about 2.31 times that of pure ZCS (Fig. 3a). Compared with previously reported sulfide-based photocatalysts for H_2O_2 production, our as-prepared Zn_V-ZCS-10 exhibits excellent photocatalytic performance for H_2O_2 generation (Table S2). The enhanced activity suggests that introducing Zn vacancies effectively promotes H_2O_2 photosynthesis over ZCS. Fig. 3b shows the average H_2O_2 yields of the Zn_V-ZCS-X (where X represents the amount of L-cysteine used) samples after 1 h of irradiation, with error bars representing the standard deviation of three independent experiments. The results indicate that the optimal performance, reaching 44.39 mmol/g, is achieved when the amount of L-cysteine is 10 mmol. Fig. 3c shows the H_2O_2 production performance of Zn_V-ZCS-10 in different atmospheres. The H_2O_2 production can hardly be detected under an argon atmosphere, however, obvious catalytic activity can be observed in air and pure oxygen atmosphere, and the production amount in pure oxygen atmosphere is higher, which further demonstrates that O_2 is the dominant feedstock involved in photocatalytic H_2O_2 production. The AQY experiment (The specific methods can be found in the Supplementary Files) results (Fig. 3d) further reveal the wavelength-dependent photocatalytic performance of Zn_V-ZCS-10. The AQY increases from 6.31% at 365 nm to 10.33% at 425 nm, indicating that Zn_V-ZCS-10 exhibits the highest quantum efficiency in the 365–425 nm wavelength range. When the wavelength further increases to 520 and 920 nm, the AQY sharply decreases to 0.62% and 0.006%, suggesting that long-wavelength light contributes negligibly to the photocatalytic reaction. After five cycles, Zn_V-ZCS-10 still retains more than 78% of its initial activity, indicating acceptable photocatalytic stability (Fig. 3e). Additionally, we measured the XRD patterns and SEM images (Fig. S1) of the Zn_V-ZCS-10 samples before and after cycling. No significant

changes can be observed from the results, indicating that the as-prepared catalyst possesses good structural stability.

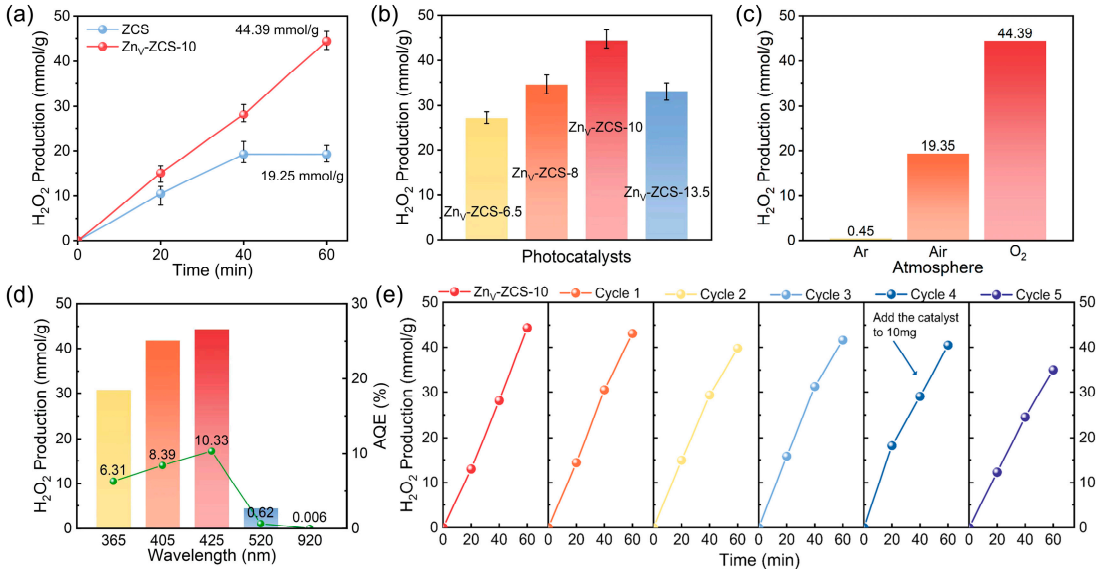

Figure 3: (**a**) Time-dependent photocatalytic H_2O_2 production over ZCS and Zn_V-ZCS-10 (the error bars represent the standard deviation of three independent experiments); (**b**) Photocatalytic H_2O_2 production over Zn_V-ZCS-X samples with different amounts of L-cysteine (The error bars represent the standard deviation of three independent experiments); (**c**) Photocatalytic H_2O_2 production over Zn_V-ZCS-10 under different atmospheres (Ar, Air, O_2); (**d**) Photocatalytic H_2O_2 production and AQY over Zn_V-ZCS-10 at different irradiation wavelengths; (**e**) Performance of Zn_V-ZCS-10 for photocatalytic H_2O_2 production in five successive runs.

2.3 Optoelectronic Properties

To study how Zn vacancies affect the optical properties of ZCS, solid-state UV-Vis diffuse reflectance spectroscopy (UV-Vis DRS) was used to test ZCS and Zn_V-ZCS-10. The UV–vis DRS spectra (Fig. 4a) indicate that both samples possess pronounced light-harvesting capability in the visible region, while Zn_V-ZCS-10 shows overall stronger absorption in the 400–800 nm range, suggesting that the engineering of Zn vacancies enhances the ZCS light-harvesting capability. According to the Kubelka-Munk transformation and the Tauc plot fitting (inset of Fig. 4a), the ZCS optical band gap is about 2.17 eV. The band gap value for Zn_V-ZCS-10 is about 2.05 eV. The conduction band potential of Zn_V-ZCS-10 is about −0.60 V (vs. NHE), which is slightly more positive than that of ZCS (−0.73 V). Nevertheless, it remains more negative than the redox potential of $O_2/\cdot O^{2-}$ (−0.33 V vs. NHE), indicating that the photogenerated electrons still have sufficient thermodynamic driving force to reduce O_2 to $\cdot O^{2-}$. Therefore, the enhanced photocatalytic H_2O_2 production of Zn_V-ZCS-10 should not be simply attributed to a more negative CB position, but rather to the combined effects of improved charge separation, increased carrier concentration, reduced interfacial charge-transfer resistance, and facilitated O_2 activation induced by Zn vacancies. The Mott-Schottky plots (Fig. 4c) show positive slopes. This shows both samples are n-type semiconductors. Under the same conditions, Zn_V-ZCS-10 has a much smaller slope than ZCS. From the Mott-Schottky equation, the slope of the $1/C^2$-V curve is inversely related to the donor density (N_D) [40]. A smaller slope means a higher carrier concentration in Zn_V-ZCS-10. The electrical properties were tested with an electrochemical workstation. The transient photocurrent curves (Fig. 4d) show Zn_V-ZCS-10 gives a higher and more stable photocurrent under on-off 425 nm light.

Electrochemical impedance spectroscopy (EIS) results (Fig. 4e) show that Zn_V-ZCS-10 presents a markedly reduced Nyquist semicircle compared with ZCS. This indicates that the interfacial charge transfer resistance is lower. Linear sweep voltammetry (LSV, Fig. S3c) under light shows Zn_V-ZCS-10 has higher photocurrent densities in the tested potential range. In the dark, both samples show very low current. This indicates that the process is mainly driven by light. The photocurrent trend is similar to the photocatalytic activity. Photoluminescence (PL) spectra (Fig. 4f) show Zn_V-ZCS-10 has much lower emission intensity than ZCS. The presence of Zn vacancies is beneficial for inhibiting charge-carrier recombination while enhancing charge separation. The optical and electrochemical results show that Zn_V-ZCS-10 has a smaller band gap, a higher carrier concentration, and lower interfacial charge transfer resistance. This contributes to enhancing the photocatalytic H_2O_2 production.

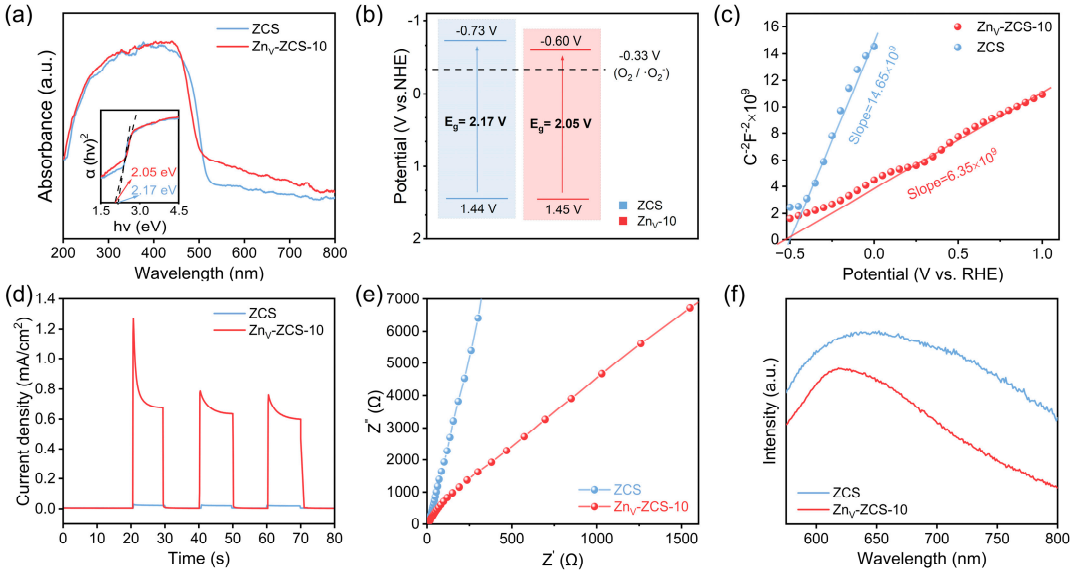

Figure 4: (**a**) UV-Vis diffuse reflectance spectra of the synthesized ZCS and Zn_V-ZCS-10; (**b**) Band structures of ZCS and Zn_V-ZCS-10; (**c**) Mott–Schottky plots of ZCS and Zn_V-ZCS-10; (**d**) Transient photocurrent spectra of ZCS and Zn_V-ZCS-10; (**e**) Electrochemical impedance spectroscopy spectra (EIS); (**f**) Photoluminescence (PL) spectra of ZCS and Zn_V-ZCS-10 (excitation wavelength: 525 nm).

2.4 Mechanistic Investigation of Photocatalytic H_2O_2 Production

To elucidate the photocatalytic H_2O_2 generation mechanism over Zn_V-ZCS-10, radical trapping and EPR experiments were performed. As shown in Fig. 5a, the H_2O_2 yield decreased sharply from 44.39 to 3.05 mmol/g after adding p-benzoquinone (p-BQ), demonstrating that $\cdot O_2^-$ is the dominant intermediate. By contrast, tert-butanol and β-carotene only caused slight inhibition, suggesting that ·OH and $^1O_2$ are not the major reactive species. In addition, the decreased H_2O_2 yield in the presence of KPS, an electron scavenger, confirms that photogenerated electrons are indispensable for O_2 reduction and subsequent $\cdot O_2^-$ formation [41]. The time-dependent EPR spectra further show gradually enhanced DMPO-$\cdot O_2^-$ signals under irradiation, directly verifying the continuous generation of $\cdot O_2^-$. Based on these results, the H_2O_2 generation over Zn_V-ZCS-10 primarily proceeds through a $\cdot O_2^-$-mediated two-step single-electron oxygen reduction pathway, as illustrated in Fig. 5c. After introducing Zn vacancies into ZCS, although the conduction band position is lowered, it still satisfies the thermodynamic requirement for O_2 to obtain electrons and be reduced to $\cdot O_2^-$. Upon light irradiation, electrons in the valence band of Zn_V-ZCS-10 are excited to the conduction band. Photocurrent and PL results indicate that the presence of Zn vacancies

endows Zn_V-ZCS-10 with higher charge carrier separation efficiency than pristine ZCS, thereby generating more photogenerated electrons. Furthermore, XPS analysis reveals that the Zn vacancies on the surface of Zn_V-ZCS-10 can modulate the electronic structure of the active S sites, thereby accelerating the rate of H_2O_2 production via the two-step single-electron O_2 reduction pathway. Meanwhile, the photogenerated holes left in the valence band are effectively consumed by the sacrificial agent.

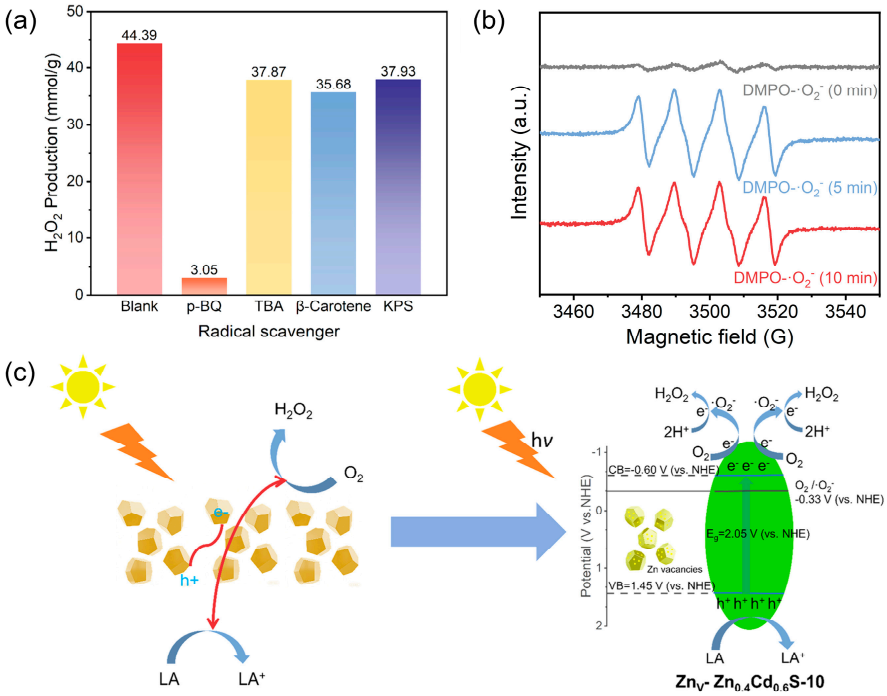

Figure 5: (**a**) Photocatalytic H_2O_2 production over Zn_V-ZCS-10 with different radical scavengers; (**b**) EPR spectra of DMPO-·O_2^- adducts over Zn_V-ZCS-10 at different irradiation times; (**c**) Proposed photocatalytic mechanism for H_2O_2 production over Zn_V-ZCS-10.

3 Conclusion

In this work, Zn vacancy-engineered $Zn_{0.4}Cd_{0.6}S$ photocatalysts (Zn_V-ZCS) were successfully prepared through a hydrothermal strategy by utilizing the coordination interaction between Zn^{2+} ions and the thiol group of L-cysteine. The optimized Zn_V-ZCS-10 sample delivered an H_2O_2 production yield of 44.39 mmol/g within 1 h, showing a 2.31-fold enhancement relative to pristine ZCS. Zn-vacancy engineering did not disrupt the crystal structure of ZCS, but it markedly improved charge behavior by promoting electron separation, increasing electron availability, and decreasing interfacial transfer resistance, ultimately leading to more efficient use of photogenerated electrons. More importantly, adding Zn vacancies changes the local electronic structure of the catalyst. This change facilitates the catalyst convert O_2 into superoxide radicals ($\cdot O_2^-$). The $\cdot O_2^-$ then reacts with H^+ to form H_2O_2. This work demonstrates that creating cation vacancies is an effective strategy to control charge carrier behavior. It also provides a simple strategy for designing sulfide photocatalysts with better performance for photocatalytic H_2O_2 production.

Acknowledgement: Not applicable.

Funding Statement: This work was supported by the Jiangsu Provincial College Students' Innovation and Entrepreneurship Training Program (202510299084).

Author Contributions: The authors confirm contribution to the paper as follows: Conceptualization, Yuanyi Zhang and Jing Xu; methodology, Yuanyi Zhang and Zhenyu Wang; validation, Yuanyi Zhang, Yang Gu and Yuxin Lan; formal analysis, Yuanyi Zhang and Wei Yan; resources, Jing Xu; data curation, Yuanyi Zhang; writing—original draft preparation, Yuanyi Zhang; writing—review and editing, Jing Xu and Yingcong Wei; visualization, Yuanyi Zhang and Yang Gu; supervision, Jing Xu; project administration, Jing Xu; funding acquisition, Jing Xu. All authors reviewed and approved the final version of the manuscript.

Availability of Data and Materials: The datasets generated during and/or analyzed during the current study are available from the corresponding author on reasonable request.

Ethics Approval: Not applicable.

Conflicts of Interest: The authors declare no conflicts of interest.

Supplementary Materials: The supplementary material is available online at https://www.techscience.com/doi/10.32604/cl.2026.082986/s1.

References

1. Jiang Z, Li C, Qi F, Wang Z, Liu Y, Li F, et al. A review on photocatalytic hydrogen peroxide production from oxygen: material design, mechanisms, and applications. ACS Appl Mater Interfaces. 2025;17(1):42–66. [CrossRef].
2. Wang W, Gu W, Li G, Xie H, Wong PK, An T. Few-layered tungsten selenide as a co-catalyst for visible-light-driven photocatalytic production of hydrogen peroxide for bacterial inactivation. Environ Sci Nano. 2020;7(12):3877–87. [CrossRef].
3. Wen C, Zhang J, Feng Y, Duan Y, Ma H, Zhang H. Purification and identification of novel antioxidant peptides from watermelon seed protein hydrolysates and their cytoprotective effects on H_2O_2-induced oxidative stress. Food Chem. 2020;327:127059. [CrossRef].
4. Abdelshafy AM, Neetoo H, Al-Asmari F. Antimicrobial activity of hydrogen peroxide for application in food safety and COVID-19 mitigation: an updated review. J Food Prot. 2024;87(7):100306. [CrossRef].
5. Lin YJ, Khan I, Saha S, Wu CC, Barman SR, Kao FC, et al. Thermocatalytic hydrogen peroxide generation and environmental disinfection by Bi_2Te_3 nanoplates. Nat Commun. 2021;12(1):180. [CrossRef].
6. Li X, Wu K, Chen S, Yuan B, Wang J, Tang C, et al. Hydrogen peroxide-mediated tandem catalysis for electrifying chemical synthesis. Chem Catal. 2024;4(8):100997. [CrossRef].
7. Chen Z, Yao D, Chu C, Mao S. Photocatalytic H_2O_2 production Systems: design strategies and environmental applications. Chem Eng J. 2023;451:138489. [CrossRef].
8. Wang X, Shao Y, Pan J, Jiang D, Cong Y, Lv SW. Exploring the green technique based on photocatalysis to produce hydrogen peroxide: progress and challenge. Chem Eng J. 2024;490:151923. [CrossRef].
9. Ding L, Pan Z, Wang Q. 2D photocatalysts for hydrogen peroxide synthesis. Chin Chem Lett. 2024;35(12):110125. [CrossRef].
10. Freese T, Meijer JT, Feringa BL, Beil SB. An organic perspective on photocatalytic production of hydrogen peroxide. Nat Catal. 2023;6(7):553–8. [CrossRef].
11. Wang Y, Xu T, Zhang Z, Wang Y, Huang J, Xue P, et al. Photocatalytic synthesis of hydrogen peroxide: recent advances, challenges, and future perspectives. Nanoscale. 2025;17(30):17443–79. [CrossRef].
12. Yang Z, Wang J. Highly efficient photocatalytic H_2O_2 production over a $Zn_{0.3}Cd_{0.7}S$/MXene photocatalyst for degradation of emerging pollutants under visible-light irradiation. Langmuir. 2024;40(6):3168–80. [CrossRef].
13. Zhou W, Zhang Y, Li B, Jiang J, Liu Q. Advances in constructing efficient photocatalytic systems for hydrogen peroxide production: insights from synchrotron radiation research. Artif Photosynth. 2025;1(4):156–73. [CrossRef].
14. Nosaka Y, Nosaka AY. Generation and detection of reactive oxygen species in photocatalysis. Chem Rev. 2017;117(17):11302–36. [CrossRef].
15. Hamdan S, Al-Ali K, Vega LF, Muscetta M, Yusuf AO, Palmisano G. Zinc cadmium sulphide ($Zn_xCd_{1-x}S$)-based photocatalysts for hydrogen production from seawater and wastewater. J Environ Chem Eng. 2024;12(5):113937. [CrossRef].

16. Li Q, Meng H, Zhou P, Zheng Y, Wang J, Yu J, et al. $Zn_{1-x}Cd_xS$ solid solutions with controlled bandgap and enhanced visible-light photocatalytic H2-production activity. ACS Catal. 2013;3(5):882–9. [CrossRef].
17. Li K, Chen R, Li SL, Xie SL, Dong LZ, Kang ZH, et al. Engineering $Zn_{1-x}Cd_xS$/CdS heterostructures with enhanced photocatalytic activity. ACS Appl Mater Interfaces. 2016;8(23):14535–41. [CrossRef].
18. Kudo A, Miseki Y. Heterogeneous photocatalyst materials for water splitting. Chem Soc Rev. 2009;38(1):253–78. [CrossRef].
19. Chen M, Hou W, Chen C, Wang Y, Xu Y. Wavelength-dependent photoactivity of Zn_xCd_{1-x} S and $ZnCo_2O_4$/Zn x Cd_{1-x} S for H_2 and H_2O_2 production. Int J Hydrogen Energy. 2022;47(39):17241–51. [CrossRef].
20. Feng C, Zhang L. Microdroplet assisted hollow ZnCdS@PDA nanocages' synergistic confinement effect for promoting photocatalytic H_2O_2 production. Mater Horiz. 2024;11(6):1515–27. [CrossRef].
21. Wang Z, Lu D, Kondamareddy KK, He Y, Gu W, Li J, et al. Recent advances and insights in designing $Zn_xCd_{1-x}S$-based photocatalysts for hydrogen production and synergistic selective oxidation to value-added chemical production. ACS Appl Mater Interfaces. 2024;16(37):48895–926. [CrossRef].
22. Wang X, Liu B, Ma S, Zhang Y, Wang L, Zhu G, et al. Induced dipole moments in amorphous ZnCdS catalysts facilitate photocatalytic H_2 evolution. Nat Commun. 2024;15:2600. [CrossRef].
23. Zhang J, Zhang J, Sun C, Yu H, Yu J, Fedin MV, et al. An efficient S-scheme Tb-BPY COF/ZnCdS heterojunction for visible-light H_2O_2 production. Chem Commun. 2025;61(85):16608–11. [CrossRef].
24. Wang Y, Gao S, Yang J, Xiong K, Guo M, Lu T, et al. Construction of ZnCdS/C_3N_4S-scheme heterojunction for superior photocatalytic H_2O_2Production and benzylamine coupling. Adv Funct Mater. 2026;36(7):e17495. [CrossRef].
25. Khan S, Qaiser MA, Ahmad Qureshi W, Haider SN, Yu X, Wang W, et al. Photocatalytic hydrogen peroxide production: advances, mechanistic insights, and emerging challenges. J Environ Chem Eng. 2024;12(5):114143. [CrossRef].
26. Kim S, Lee S, Gu M. Efficient photocatalytic H_2O_2 generation utilizing surface functional duality in carbon dots-polydopamine heterojunctions. J Mater Chem A. 2025;13(35):29404–14. [CrossRef].
27. Zhu Q, Su J, Lin G, Li G, Zhuo Z, Wang W, et al. Surface indium vacancies promote photocatalytic H_2O_2 production over In_2S_3. Nat Commun. 2025;16:10501. [CrossRef].
28. Chen G, Lin C, Han F, Zhang H, Zhou S, Yang F, et al. Recent advances in photocatalytic H_2O_2 production: modification strategies of 2D materials and *in situ* application of H_2O_2. Mater Horiz. 2025;12(15):5492–512. [CrossRef].
29. Hao X, Wang Y, Zhou J, Cui Z, Wang Y, Zou Z. Zinc vacancy-promoted photocatalytic activity and photostability of ZnS for efficient visible-light-driven hydrogen evolution. Appl Catal B Environ. 2018;221:302–11. [CrossRef].
30. Chen C, Wang C, Zhang Y, Sun H, Xu J, Zhang Y, et al. Enhancing photocatalytic H_2O_2 production through the improvement of water oxidation via a novel lattice-oxygen-involved pathway. Appl Catal B Environ Energy. 2024;348:123854. [CrossRef].
31. Ding W, Yuan S, Yang Y, Li X, Luo M. Defect engineering: the role of cationic vacancies in photocatalysis and electrocatalysis. J Mater Chem A. 2023;11(44):23653–82. [CrossRef].
32. Yu K, Huang HB, Wang JT, Liu GF, Zhong Z, Li YF, et al. Engineering cation defect-mediated Z-scheme photocatalysts for a highly efficient and stable photocatalytic hydrogen production. J Mater Chem A. 2021;9(12):7759–66. [CrossRef].
33. Wang Z, Xiao M, You J, Liu G, Wang L. Defect engineering in photocatalysts and photoelectrodes: from small to big. Acc Mater Res. 2022;3(11):1127–36. [CrossRef].
34. Nie Y, Bo T, Zhou W, Hu H, Huang X, Wang H, et al. Understanding the role of Zn vacancy induced by sulfhydryl coordination for photocatalytic CO_2 reduction on $ZnIn_2S_4$. J Mater Chem A. 2023;11(4):1793–800. [CrossRef].
35. Xin X, Li Y, Zhang Y, Wang Y, Chi X, Wei Y, et al. Large electronegativity differences between adjacent atomic sites activate and stabilize $ZnIn_2S_4$ for efficient photocatalytic overall water splitting. Nat Commun. 2024;15(1):337. [CrossRef].
36. Lai J, Ding L, Fan C, Wei J, Qian J, Wang K. Zinc vacancy mediated electron–hole separation in ZnO nanorod arrays for high-sensitivity organic photoelectrochemical transistor aptasensor. Chem Commun. 2023;59(1):75–8. [CrossRef].

37. Idriss H. On the wrong assignment of the XPS O1s signal at 531–532 eV attributed to oxygen vacancies in photo- and electro-catalysts for water splitting and other materials applications. Surf Sci. 2021;712:121894. [CrossRef].
38. Krishnan P, Liu M, Itty PA, Liu Z, Rheinheimer V, Zhang MH, et al. Characterization of photocatalytic TiO_2 powder under varied environments using near ambient pressure X-ray photoelectron spectroscopy. Sci Rep. 2017;7:43298. [CrossRef].
39. Chen Z, Kronawitter CX, Waluyo I, Koel BE. Investigation of water dissociation and surface hydroxyl stability on pure and Ni-modified CoOOH by ambient pressure photoelectron spectroscopy. J Phys Chem B. 2018;122(2):810–7. [CrossRef].
40. Wang X, Maeda K, Thomas A, Takanabe K, Xin G, Carlsson JM, et al. A metal-free polymeric photocatalyst for hydrogen production from water under visible light. Nat Mater. 2009;8(1):76–80. [CrossRef].
41. Li J, Huang J, Zeng G, Zhang C, Yu H, Wan Q, et al. Efficient photosynthesis of H_2O_2 via two-electron oxygen reduction reaction by defective g-C_3N_4 with terminal cyano groups and nitrogen vacancies. Chem Eng J. 2023;463:142512. [CrossRef].